Upper atmosphere of Mars up to 120 km: Mars Global Surveyor accelerometer data analysis with the LMD general circulation model

M. Angelats i Coll and F. Forget
Laboratoire de Météorologie Dynamique, CNRS, Université Paris 6, Paris, France

M. A. López-Valverde
Instituto de Astrofísica de Andalucía, Granada, Spain

P. L. Read and S. R. Lewis
Atmospheric, Oceanic and Planetary Physics, University of Oxford, Oxford, UK

Received 24 July 2003; revised 22 October 2003; accepted 26 November 2003; published 28 January 2004.

[1] Mars Global Surveyor (MGS) aerobraking accelerometer density measurements are analyzed with the use of the general circulation model (GCM) at the Laboratoire de Météorologie Dynamique (LMD). MGS constant altitude density data are used, obtaining longitudinal wavelike structures at fixed local times which appear to be dominated by low zonal wave number harmonics. Comparisons with simulated data for different seasons and latitudinal bands at constant altitude are performed. Excellent agreement is obtained between the simulated and observational data for low latitudes, with accuracy in both mean and zonal structure. Higher latitudes show a reduction in agreement between GCM results and MGS data. Comparisons that result in good agreement with the observational data allow for the study of wave composition in the MGS data. In particular, the excellent agreement between the simulations and the data obtained at 115 km during areocentric longitude Ls $\approx 65^\circ$ allows the extraction of the major contributors to the signature, with the eastward propagating diurnal waves of wave numbers one to three being the major players. Significant contributions are also obtained for eastward propagating semidiurnal waves of wave numbers two, three, and five and diurnal wave number five. A sensitivity study is performed to delineate the effects of the near-IR tidal forcing of the upper atmosphere on the wave content at those heights. Simulations without this forcing yield reduced amplitudes for diurnal eastward propagating waves two and three along with a more latitudinally symmetric response for these two components as well as for diurnal eastward propagating wave number one. *INDEX TERMS:* 5409 Planetology: Solid Surface Planets: Atmospheres—structure and dynamics; 3384 Meteorology and Atmospheric Dynamics: Waves and tides; 6225 Planetology: Solar System Objects: Mars; *KEYWORDS:* upper atmosphere, Mars, waves, nonlinear, MGS

Citation: Angelats i Coll, M., F. Forget, M. A. López-Valverde, P. L. Read, and S. R. Lewis (2004), Upper atmosphere of Mars up to 120 km: Mars Global Surveyor accelerometer data analysis with the LMD general circulation model, *J. Geophys. Res.*, *109*, E01011, doi:10.1029/2003JE002163.

1. Introduction

[2] Mars Global Surveyor (MGS) aerobraking phases, required to achieve its mapping orbit, have yielded thermospheric densities, scale heights and temperatures covering a broad range of local times, seasons and spatial coordinates [*Keating et al.*, 1998, 2001]. Periapsis data during aerobraking covered different seasons, latitude bands and local times for the two phases. The longitudinal sampling of the spacecraft is however complete. Phase I covered local times from 11 to 16 h (assuming 24 "Martian hours" per Martian day or sol), with a latitude coverage of approximately 40° to 60°N. Seasons observed during this phase were centered around winter solstice and altitudes of periapsis range from 115 to 135 km. The altitudes for Phase II were lower, with a minimum around 100 km. Martian spring was the season covered during this phase and the local time was between 15 and 16 h. The latitude band covered by Phase II, however, was more extensive than that seen during Phase I, with a coverage from 60°N to basically the South Pole. The local time and latitude distribution of the data coverage is depicted in Figure 1.

[3] MGS density data above 110 km as sampled at a fixed local time yield large amplitude longitudinal variations composed of a variety of wave numbers (*s*) which are

0148-0227/04/2003JE002163$09.00

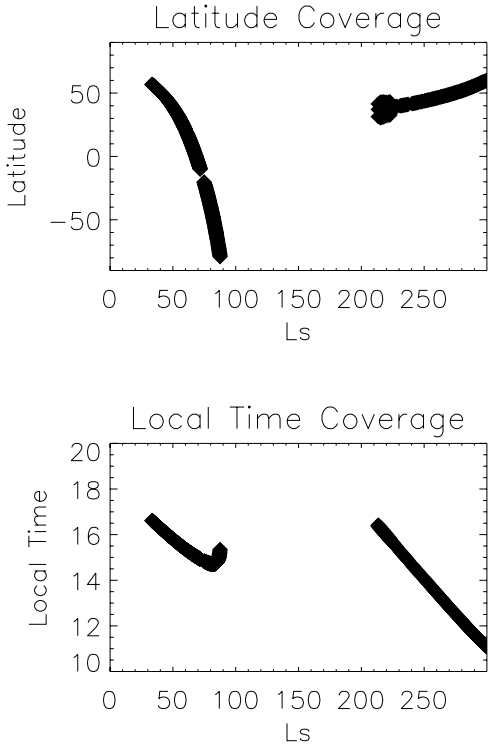

Figure 1. MGS latitudinal and local time coverage as a function of areocentric longitude used in this study.

characterized by large $s = 2$ component and smaller $s = 1$ and $s = 3$ contributions. These oscillations were first interpreted as possible stationary planetary waves [*Keating et al.*, 1998], while it has been later suggested that eastward propagating waves of diurnal frequency, specifically diurnal Kelvin waves, could be responsible for the density signature [*Forbes and Hagan*, 2000; *Wilson*, 2000, 2002; *Bougher et al.*, 2001].

[4] Any sampling of the atmosphere will undoubtedly reflect the vast array of existing waves, and the signature obtained will be the result of a combination of them. For a fixed local time sampling of the atmosphere, determining the dominant waves in the sampled signature can be an impossible feat from the observations alone. The multiple possibilities of waves that can generate a given signature when sampled at a fixed local time can be seen from the expression for a wave in a local time frame of reference:

$$A \cdot \cos[(s + 24/p)\lambda - \sigma t_{LT} - \phi] \tag{1}$$

where A is the amplitude, s the wave number, p the period in hours, λ the east longitude, σ the frequency ($\sigma = 2\pi/p$), t_{LT} the local time in hours and ϕ the phase of the wave. This formulation uses the convention of westward (eastward) propagating waves having negative (positive) wave numbers, with all waves having positive frequencies. As can be seen from this expression, waves that propagate to the west with the apparent motion of the sun will yield a constant value and no longitudinal variation when sampled at a fixed local time. With a phase speed of $-\frac{2\pi}{24}$ (h^{-1}) and periods that are subharmonic of a day, these migrating tides would be represented by the following wave number/period pair ($s = -n$, $p = 24/n$) where n is any given wave number. Only nonmigrating tides will contribute to a longitudinal structure at a given local time.

[5] By nonmigrating tides, one refers to those oscillations that have periods that are subharmonics of a day, but their phase speed $\left(\frac{\sigma}{s}\right)$ differs from the migrating tide's value of $-\frac{2\pi}{24}$ (h^{-1}). These oscillations, in contrast to the westward migrating tides, can have eastward or westward propagation with respect to the sun, or be standing. Nonmigrating tides can be directly forced through longitudinal variations in solar heating, or arise as the outcome of a nonlinear interaction between other preexisting waves. Variations with longitude of solar heating absorption would be the result of a modulation through topography or species concentrations as the incoming solar radiation has no longitudinal dependence at the top of the atmosphere. The nonlinear mechanism works as follows: Given an oscillation composed of two waves with frequencies σ_1 and σ_2 and wave numbers s_1 and s_2, a quadratic system operating on the wave (such as the nonlinear terms in the momentum equations) would yield the original primary waves plus four other secondary ones, as shown in the following equations [*Teitelbaum and Vial*, 1991]:

$$X = \cos(s_1\lambda - \sigma_1 t) + \cos(s_2\lambda - \sigma_2 t) \tag{2}$$

$$X^2 = 1 + \frac{1}{2}[\cos(2s_1\lambda - 2\sigma_1 t) + \cos(2s_2\lambda - 2\sigma_2 t)] + \cos([s_1 + s_2]\lambda - [\sigma_1 + \sigma_2]t) + \cos([s_1 - s_2]\lambda - [\sigma_1 - \sigma_2]t) \tag{3}$$

These secondary waves, as can be seen, have the following frequency-wave number pairs: ($2\sigma_1$, $2s_1$), ($2\sigma_2$, $2s_2$), ($\sigma_1 + \sigma_2$, $s_1 + s_2$) and ($\sigma_1 - \sigma_2$, $s_1 - s_2$). This process has been shown to be relevant in the Earth's atmosphere to explain the presence of a westward-propagating semidiurnal $s = -1$ oscillation over the South Pole [*Forbes et al.*, 1995; *Angelats i Coll and Forbes*, 2002]. On Mars, the large topographic relief is dominated by the zonal wave number two component at low latitudes and can modulate the thermal forcing of the migrating tides, thus generating nonmigrating components. The interaction of the topographic component $\cos(m\lambda)$ with the thermal tidal forcing $\cos(s\lambda - \frac{2\pi}{24}st)$ will yield the modulated forcing $\cos((s \pm m)\lambda - \frac{2\pi}{24}st)$ in a similar manner as described above [*Forbes and Hagan*, 2000]. Effects of the longitudinally inhomogeneous Martian surface on the tidal response were first studied by *Conrath* [1976] and *Zurek* [1976], and both found that the large zonal wave number two component of the topography induced an eastward propagating zonal wave number one Kelvin wave through its modulation of the migrating diurnal tidal forcing. This outcome can be seen from the expression of the modulated forcing above with $s = -1$ for the migrating diurnal tide and $m = 2$ for the component of planetary relief, which yields $s + m = 1$ and a period of 24 hours. Further and more detailed study of Kelvin wave response is given by *Wilson and Hamilton* [1996]. From the nonlinear process described in equations (2) and (3), one can also see that the interaction of a stationary planetary wave with the diurnal migrating tide

will also lead to nonmigrating tides, and more specifically to diurnal Kelvin waves. The relevance of this process, that could occur at high altitude, has not as yet been determined and further work on this issue is required.

[6] MGS through its aerobraking phases has provided much needed data on the upper atmosphere of Mars, allowing for comparison and validation of GCM models. It is through this comparison and analysis of the simulated data that a clearer vision of the dynamics of the atmosphere of Mars can develop. This is the approach taken in this paper in that we compare LMD GCM model results with MGS accelerometer data from Phase I and II in the upper atmosphere. Interesting wave structures observed in situ and reproduced in the numerical simulations are analyzed to determine the present dominant waves and their possible origin. A sensitivity study of the results is later performed to ascertain the importance of various atmospheric processes, such as the upper atmosphere in situ forced tides.

2. GCM Simulations and MGS Data Comparisons

[7] The Mars LMD GCM has evolved from a terrestrial climate model [*Hourdin et al.*, 1993; *Forget et al.*, 1999] and has been extended to the Mars upper atmosphere through a collaboration with the University of Oxford and the Instituto de Astrofísica de Andalucía. The model extends from the ground up to a height of approximately 120 km and includes the relevant processes near the surface such as turbulent diffusion in the planetary boundary layer, convection, orography and low-level drag, all at sub-grid scales. The energetics of the simulations include the effects of the presence in the Mars atmosphere of suspended dust and CO_2. Parameterizations of thermal infrared cooling and near-infrared heating by CO_2 both account for non-LTE effects. The CO_2 condensation-sublimation cycle is also realistically included. A more detailed description of the model is given by *Forget et al.* [1999] and in the companion paper by F. Forget et al. (Upper atmosphere of Mars up to 120 km: Numerical simulation with a general circulation model, manuscript in preparation, 2003) (hereinafter referred to as Forget et al., manuscript in preparation, 2003). A description of the prescribed dust distribution employed, which yields temperatures consistent with MGS radio occultation and the Thermal Emission Spectrometer (TES), is given by Forget et al. (manuscript in preparation, 2003).

[8] MGS Accelerometer observations are used in this analysis [*Keating et al.*, 2001]. Periapsis density data were scaled to one of the four following levels: 110, 115, 120 and 130 km depending on periapsis altitude. Scaling was performed through

$$\rho_z = \rho_p \cdot \exp^{\frac{z_p - z}{H_p}}$$

with the use of the value of scale height at periapsis. We used the different altitudes for the following orbits and seasons: 130 km covers through orbit number 70 with an Ls $\approx 238°$ (only data with periapsis height above 125 km were used); 120 km spans from orbit 70 to 201 (end of Phase I) with Ls marching from 238° to 302°; 115 km starts Phase II data from orbit 582 to 930 with Ls from 33° to 73°; and 110 km covers orbits from 930 to 1220 which ranges from Ls $\approx 73°$ to Ls $\approx 90°$. The observational data were scaled within a scale height at periapsis and Table 1 summarizes the mean periapsis altitudes and mean scale heights for the four subsets of data used. Latitudinal and temporal coverage of the MGS observations used in the comparisons is summarized in Figure 1 as a function of areocentric longitude. The measurements covered from 60°N to 85°S during northern spring while the local time sampled remained between 15 and 17 h. During northern winter, latitude coverage was more restricted ranging from 40°N to 60°N, while the sampled local times varied from 11 to 16 h. Data was then sorted according to common local times at each altitude. The data obtained, where a significant number of points was available, are shown in Figures 2 and 3 along with GCM results that correspond to the observations. Simulated data used have been averaged over ten days conserving the diurnal variations in the fields. It is important to note that the model was not especially 'tuned' to MGS observations, other than the broad agreement obtained in lower atmosphere temperatures (<35 km) through the choice of a simple prescribed dust distribution (which does not vary as a function of longitude).

Table 1. Mean Periapsis Altitudes and Mean Scale Heights for the Four Subsets of Data Analyzed[a]

z	$\overline{P}$	$\overline{SH}$
130	129.401	7.79812
120	119.788	7.14154
115	113.797	7.57069
110	108.102	6.43926

[a]Units are in kilometers. Left column (z) denotes interpolated altitude; middle column ($\overline{P}$) denotes mean MGS periapsis altitude; right column ($\overline{SH}$) denotes mean MGS scale height.

[9] In general, model simulations are able to reproduce the observations with very good agreement at low to mid latitudes during the Northern Spring. Notable agreement is found at 115 km for the northern spring seasons of Ls = 30°–60° (Figure 2a) and Ls = 65° (Figure 3a). For these two cases the wave structure observed from orbit is clearly reproduced in the GCM data, and seems to be strongly composed of wave numbers 2 and 3. A detailed analysis of the wave activity responsible for the latter structure is performed in the next section. At 130 km (Figure 2b), some of the differences found could be ascribed to the high altitude of the observations, this being almost the limit of the valid simulation data since a sponge layer is included at the top of the model which begins approximately at this height. EUV solar absorption effects become relevant at thermospheric heights and are currently not included in the simulations. The absence of this process is another possible source for the differences at this height. Figures 2c and 2d show comparisons at 120 km during two dusty seasons around northern winter solstice. The agreement with the observations is rather good and slight differences can possibly be due to regional dust storm properties of the period. Comparisons at Ls $\approx 80°$ reveal a latitudinal dependence, with lesser agreement with the observations in the southern hemisphere as the latitude becomes more poleward. This can be seen in Figure 3b to 3d. From these

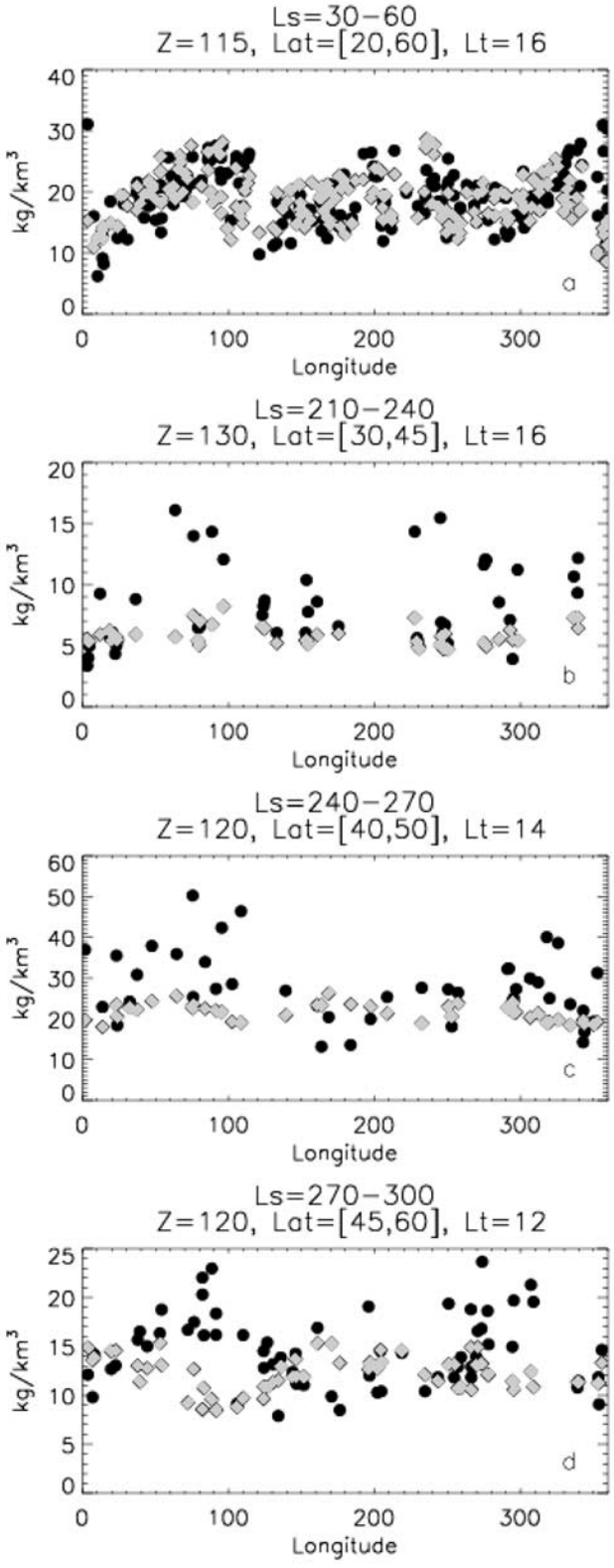

Figure 2. MGS versus LMD GCM density comparison. MGS data interpolated at the altitude Z (in km above the geoid) are represented with solid black dots, while GCM results obtained at the same location and local time are displayed in green diamonds. Units for density are kg/km^3. Season, time and location are marked for each panel. See color version of this figure in the HTML.

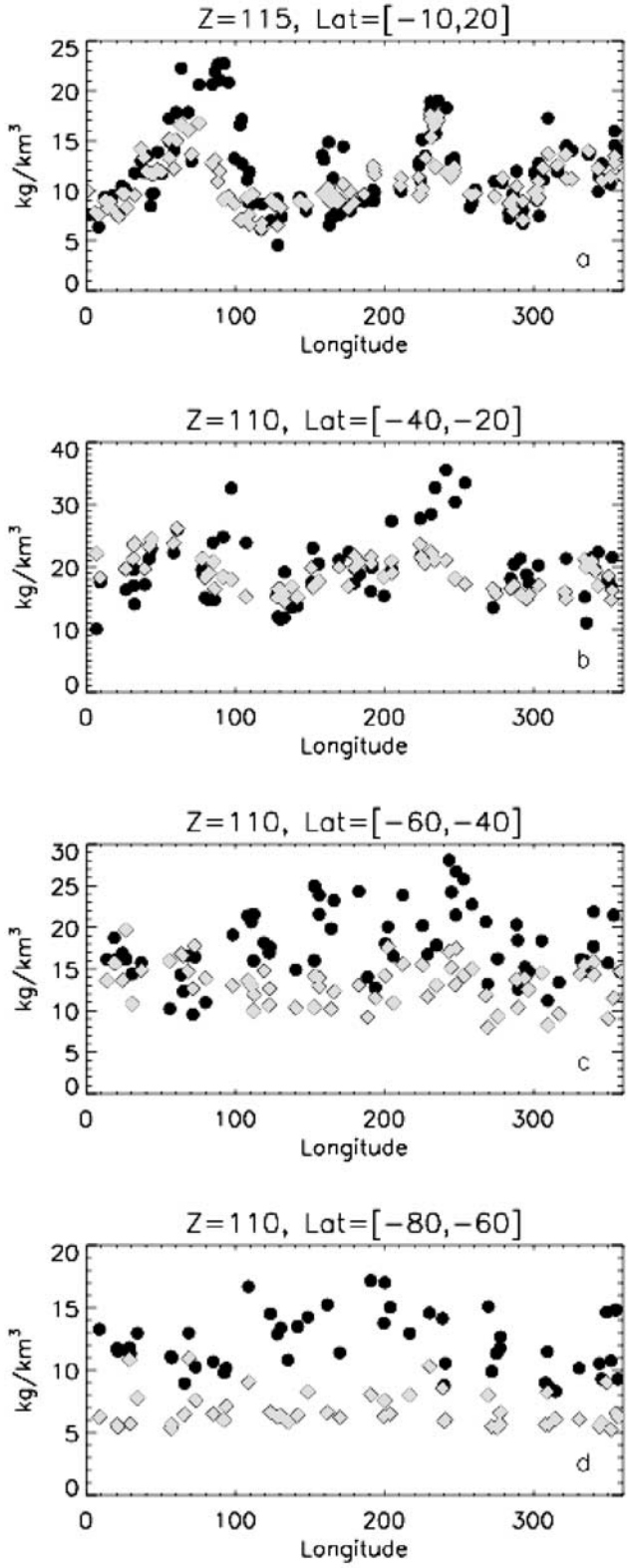

Figure 3. MGS (dot) versus LMD GCM (diamond) density comparison. As in Figure 2 but with LT = 15h and Ls ≈ 65° for panel (a) and Ls ≈ 80° for panels (b) to (d). See color version of this figure in the HTML.

three panels one can note that the GCM systematically underestimates the atmospheric density, which would indicate that it underestimates the atmospheric temperature below in the polar regions (probably in the dynamically forced inversion around 70 km [see *Forget et al.*, 1999]), and that the observational data are more scattered than the simulated data, which are averaged over ten days. A plausible explanation for these discrepancies is the large day-to-day variability that is found to exist at high southern latitudes above 90 km in the GCM simulations. The positioning of this highly variable region over the top of the eastward zonal jet is suggestive of a barotropic instability generating some of the wave activity present there. *Withers et al.* [2003] showed sol-to-sol variability in the MGS data to be below average at high latitudes and also noticed an increase of variability with decreasing altitudes across latitudes. The discrepancy in latitudinal distribution of the day-to-day variability between observations and our simulations is possibly related to the presence of gravity waves and their present parameterization in the model. This is an issue that requires further study and will not be discussed herein.

3. Wave Analysis

[10] Given the rather striking agreement obtained in several cases between MGS data and the GCM simulations for the same conditions, an analysis of the modeled data can shed some light on the wave activity at work in the upper atmosphere of Mars. Longitudinal structures similar to the ones previously shown (Figures 2 and 3) have been observed and interpreted before. In one case, the signature was initially classified as a stationary wave [*Keating et al.*, 1998] and has later been shown to be due to the presence of nonmigrating tides, and more specifically, diurnal Kelvin waves [*Forbes and Hagan*, 2000; *Wilson*, 2002]. In another instance, analysis of MGS Radio Science electron density profiles at high northern latitudes at a fixed local time resulted in a signature with a dominant wave number three component which with the use of MGS Accelerometer data would seem to have a semidiurnal frequency [*Bougher et al.*, 2001]. Such a signature, by equation (1) (with $s + 24/p = 3$ and $p = 12$), could be generated by a semidiurnal eastward propagating wave with zonal wave number one. Significant amplitudes of this latter wave at the locations of observation are obtained in the simulations by *Wilson* [2002]. For all of the nonmigrating tides just mentioned and believed to be at the origin of the observed signatures, the excitation mechanism has been suggested to lie on the modulation of the migrating tidal forcing by Mars' topography components [*Zurek*, 1976; *Wilson and Hamilton*, 1996; *Forbes and Hagan*, 2000]. A wave analysis of the LMD GCM simulation data yields other significant contributors to the detailed structures observed by MGS.

[11] The focus of our analysis is on Phase II MGS accelerometer data shown in Figure 3a, which represents equatorial latitudes (10°S–20°N) at a height of 115 km for $Ls \approx 65°$, and local time of 15 h. As can be seen, a very good agreement with the observations is obtained with the wave structure clearly represented. The data show a possible dominant combination of wave number 2 and 3 as seen in a fixed local time frame of reference, which according to equation (1) could be produced by a variety of wave number/period pairs.

[12] A space-time Fourier decomposition was performed on the GCM data to extract the prominent waves present in the simulation. The analysis was performed on ten days of simulation with wave numbers s ranging from -10 to 10 (westward and eastward, respectively) and periods from 8 to 24 hours. Stationary waves with wave numbers 1 to 6 were also examined. The obtained density amplitudes for the different wave numbers normalized by the zonal mean density are depicted in Figures 4 and 5 corresponding to diurnal and semidiurnal frequencies respectively. Magnitudes are largest for the directly forced migrating tides as expected, with significant amplitudes obtained for the diurnal eastward propagating waves with $s = 1$, 2 and 3. Lesser amplitudes are found for shorter vertical wavelength and zonally symmetric waves ($s = 0$). Semidiurnal nonmigrating tides (shown in Figure 5) have in general smaller amplitudes than those of diurnal frequency, with the $s = 1$ eastward propagating and zonally symmetric waves found to maximize above 80 km at high northern latitudes. Significant magnitudes are also seen at wave numbers two, three and five for the eastward propagating semidiurnal waves. Results here obtained are in agreement with those reported by *Wilson* [2002] using the Geophysical Fluid Dynamics Laboratory MGCM described by *Wilson and Hamilton* [1996]. The diurnal eastward propagating waves with wave number one and two can be compared with panels (a) and (b) of Figure 3 of *Wilson* [2002], respectively. Wave one shows very strong agreement between both simulations, even with the relative maximum at high southern latitudes. Wave number two wave has indeed good agreement but differences can be found in the structure at high altitudes, where a double maximum in latitude is not found in our simulated data. Regarding the semidiurnal eastward propagating wave with wave number one, both model simulations show large amplitudes at high northern latitudes but disagree elsewhere [see *Wilson*, 2002, Figure 3c]. While *Wilson* [2002] shows another maximum at high altitude at mid southern latitudes, our simulations show no signature there.

[13] Table 2 summarizes the amplitudes and phases of the waves Fourier decomposed from GCM simulations as an average over the latitude band covered by the observations in Figure 3a and an altitude of 115 km. Only waves with amplitudes over 0.16 kg/km^3, which approximately correspond to 2% value of the zonal mean at this altitude, are included. Also noted in Table 2 is the apparent wave number of the waves from a sun-synchronous reference frame, which would be the observed reference from the MGS observational point of view. The diurnal migrating tide (which would sample as zonally symmetric) yields the largest magnitude with decreasing amplitudes for the semidiurnal and terdiurnal migrating components. The largest amplitudes for nonmigrating tides are obtained for eastward propagating diurnal waves with wave numbers one, two and three (with magnitudes of 1.36, 0.99, and 1.18 kg/km^3 respectively). The amplitudes obtained for stationary waves one to three are summarized in Table 3. As can be seen, significant amplitudes are obtained at high altitude, with wave numbers two and three being dominant and of similar magnitude. These stationary waves obtained at high alti-

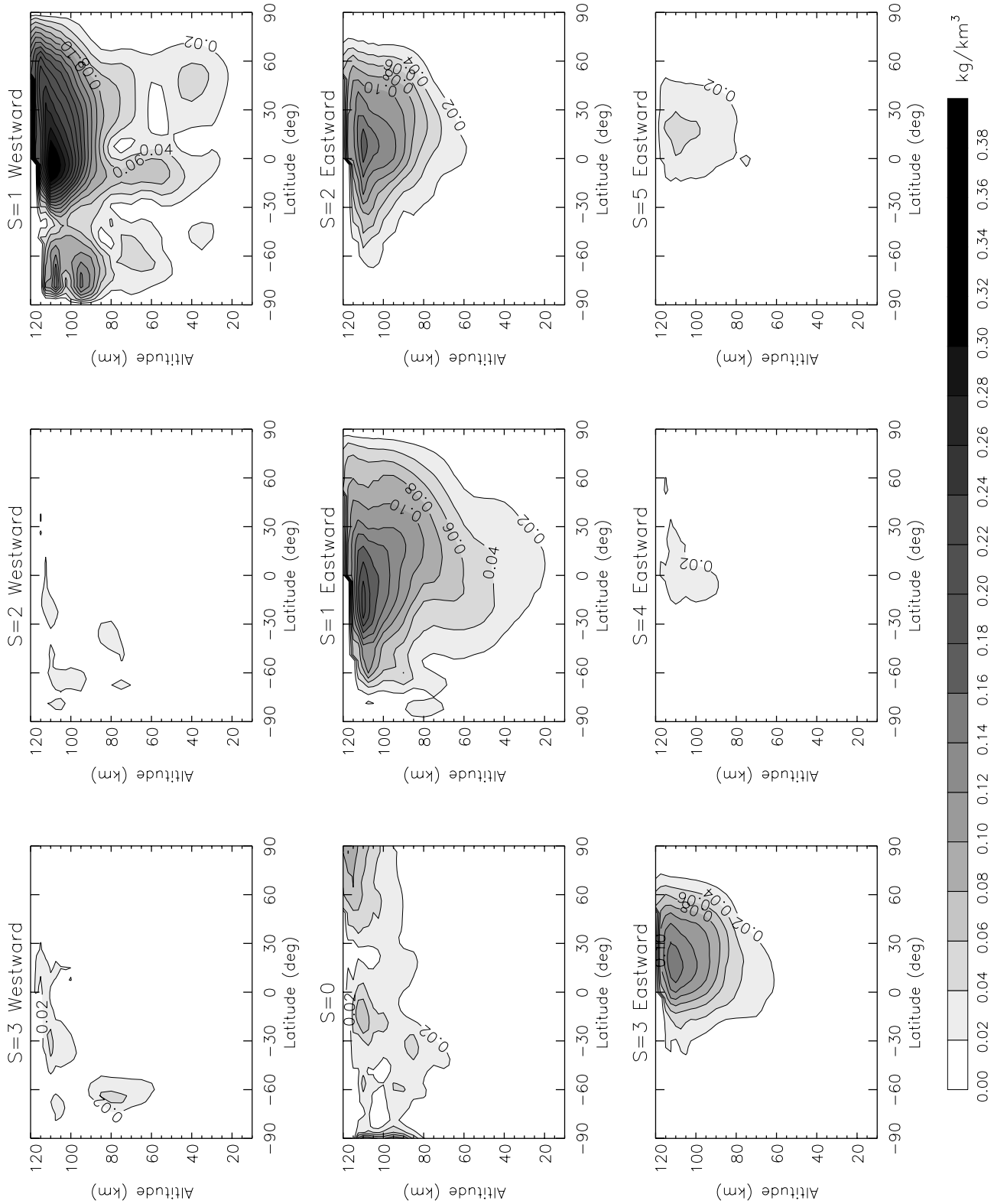

Figure 4. Relative density amplitude at $Ls \approx 65^\circ$ for diurnal frequency waves present in the simulated data. Amplitudes are normalized by local zonal mean values. Wave numbers range from westward propagating wave three ($s = -3$) to eastward propagating wave five ($s = 5$). Contour intervals are 0.02. See color version of this figure in the HTML.

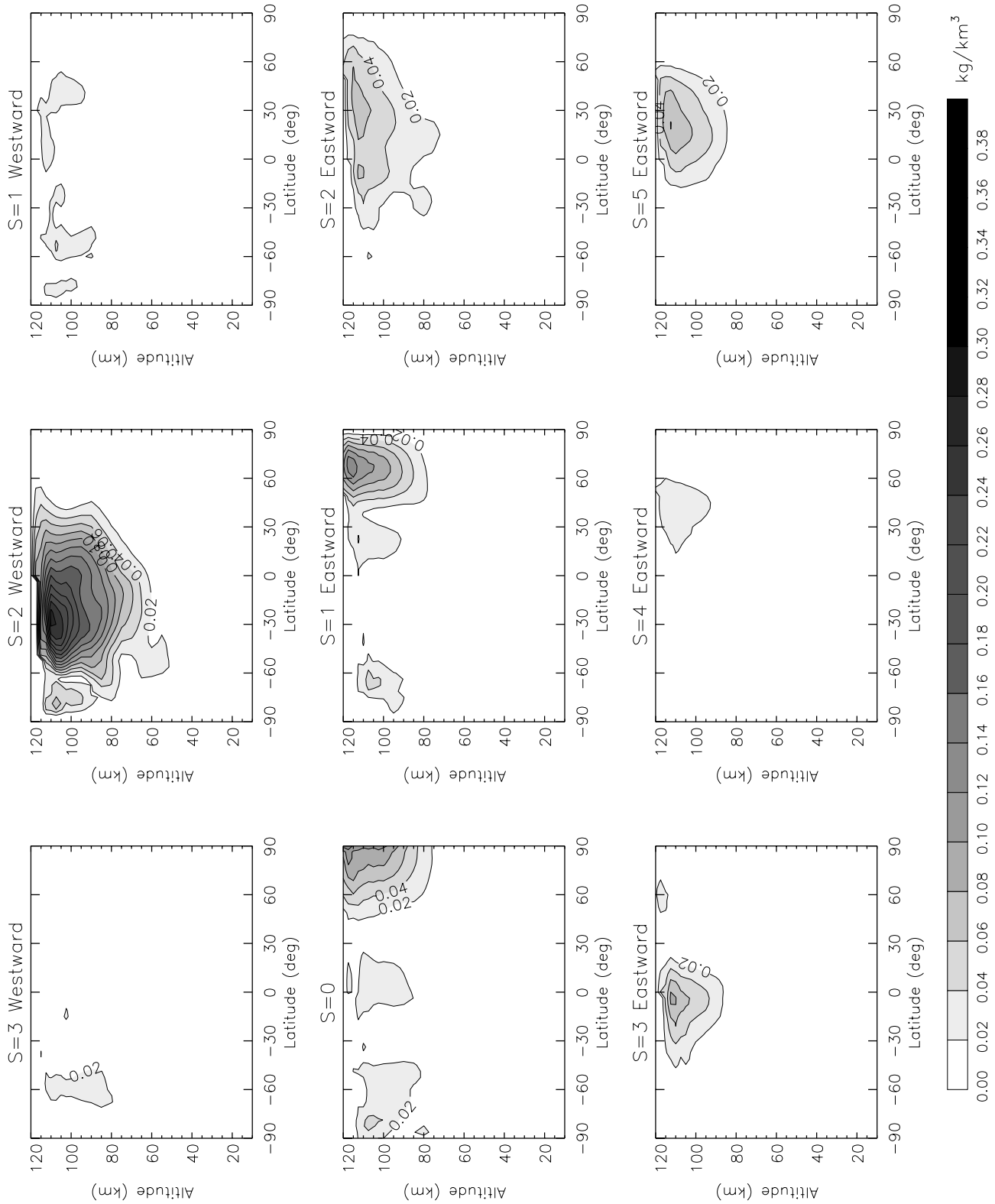

Figure 5. As in Figure 4, but for semidiurnal frequency waves. See color version of this figure in the HTML.

tudes must not correspond to those generated in the lower atmosphere since stationary waves with wave numbers two and three are not expected to propagate upward as high as that with wave number one based both on linear theory [e.g., *Andrews et al.*, 1987] and modeling results reported by *Hollingsworth and Barnes* [1996]. An explanation for the presence of these waves at high altitudes is suggested in the next subsection.

Table 2. Sample of Waves Present in the Simulations at 115 km Height[a]

s	p (h)	Amplitude	Phase (h)	s_{LT}
		Westward		
5	24	0.1916	2.60	4
4	12	0.1691	2.78	2
3	8	0.4219	−3.25	0
3	24	0.2023	−8.66	2
2	12	1.0552	−1.23	0
1	8	0.2150	0.72	2
1	12	0.2543	0.87	1
1	24	2.2478	11.59	0
		Zonally Symmetric		
0	8	0.2096	−2.37	3
0	24	0.3451	−8.12	1
		Eastward		
1	12	0.2422	1.61	3
1	24	1.3603	5.95	2
2	8	0.1691	−1.74	5
2	12	0.5346	4.44	4
2	24	0.9939	−3.30	3
3	12	0.4112	1.83	5
3	24	1.1775	−3.61	4
4	12	0.1938	2.18	6
4	24	0.2094	−7.38	5
5	12	0.4621	−3.06	7
5	24	0.3274	−8.50	6
6	8	0.1933	−1.49	9
6	12	0.1939	−4.22	8
6	24	0.1752	−4.56	7
7	12	0.2077	2.95	9

[a]Mean amplitude and phase for a latitude range of −11.25 to 22.5 corresponding to the observed MGS data. Information given is as follows: wave number (s), period in hours (p), amplitude (kg/km^3), phase in hours or degrees east longitude, and wave number in sun-synchronous reference frame (s_{LT}).

[14] The contribution of the three largest eastward propagating waves to the wave structure seen in fixed local time in Figure 3a is shown in Figure 6. The total sum of the three components is depicted in comparison with the GCM simulation data corresponding to the MGS data of Figure 3a. GCM data are here presented without contributions from the zonal mean nor migrating tides. This contribution is individually calculated for each point as the longitudinal mean at a given local time and latitude. The eastward propagating diurnal waves provide a significant portion of the structure, accounting for approximately a minimum of 50% of the extrema values. The addition of stationary wave one, two and three (not shown) does not increase significantly the closeness of the decomposition to the MGS data. The spike observed at 230°E longitude and nicely reproduced on the simulated data (Figure 3a) shows a significant contribution from the eastward propagating waves ($\sigma = 1/12$, $s = 2$), ($\sigma = 1/12$, $s = 3$), ($\sigma = 1/12$, $s = 5$), and ($\sigma = 1/24$, $s = 5$), with σ in cycles/hr. Their contribution to the observed structure is seen in Figure 6, where they have been added to the eastward diurnal $s = 1, 2, 3$ waves. As can be seen, the agreement to MGS data is significantly improved with the addition of these four waves.

[15] Latitudinal cross sections of the normalized amplitude of the three dominating eastward waves are shown in Figure 7 for an altitude of 115 km. Normalized amplitudes maximize at low latitudes with the $s = 2$ and $s = 3$ in the northern hemisphere and the $s = 1$ in the southern hemisphere. The latitudinal distribution of amplitudes for these three waves closely resembles those of Diurnal Kelvin waves, which maximize at the equator and are symmetric about it. The asymmetric distribution in latitude in the simulations hints at the presence of higher asymmetric modes of the waves that can arise through mode coupling induced by their propagation through a mean wind field that is highly asymmetric.

[16] Figure 8 shows the zonal mean winds and temperature distributions for the case at hand, and through which the aforementioned waves have propagated. Conditions close to northern summer solstice yield a strong westerly jet in the southern hemisphere with a maximum wind speed of 120 m/s. Meridional winds are southward at high altitudes as expected due to the solar-antisolar circulation induced by the in situ forcing of CO_2 absorption in the near-infrared band. The zonal mean thermal structure shows the effects of a Hadley cell that is much weaker than that during northern winter due largely to reduced solar flux near aphelion and smaller amounts of dust in the atmosphere.

4. Wave Generation

[17] As was mentioned above, nonlinear wave interactions are a viable source for nonmigrating tides when no direct forcing is at work. Here we now focus on possible nonlinear mechanisms that would induce some of the waves obtained in the simulation data. Table 4 summarized the possible interactions yielding the most dominant waves depicted in Figure 6. The complexity of GCMs makes them inconclusive for the study of such processes and a more mechanistic approach is needed to clarify its significance as a source mechanism. Here we then can only hypothesize the nature of the interactions.

[18] With this in mind, let us consider the case of the eastward propagating nonmigrating tide with diurnal period and wave number $s = 3$. It can be generated by the modulation of the diurnal tidal forcing at low altitudes by the $s = 4$ component of the topography. However, in addition to this process, another possible mechanism could be at play, i.e. the nonlinear interaction between the diurnal eastward propagating waves with wave number $s = 1$ and $s = 2$ and stationary waves with wave numbers two and one, respectively. From the discussion above on the outcomes of nonlinear interactions between different waves, one can see that two combinations are possible of period and frequency (σ, s) with the mentioned waves: ($\sigma = 1/24$, $s = 1$) + ($\sigma = 0$, $s = 2$) and ($\sigma = 1/24$, $s = 2$) + ($\sigma = 0$, $s = 1$). As the magnitude of the $s = 4$ component of the topography is rather small, and significant amplitudes were obtained for the (1/24,3) wave, the latter process could indeed be a significant player in the generation of this wave.

[19] The presence of semidiurnal nonmigrating tides in the upper atmosphere can also be speculated to be a result of

Table 3. Stationary Waves Present in the Simulations at 115 km Height[a]

s	p (h)	Amplitude	Phase (deg)	s_{LT}
1	–	0.1503	−119.99	1
2	–	0.3287	−24.85	2
3	–	0.3312	43.91	3

[a]Information given is as in Table 2.

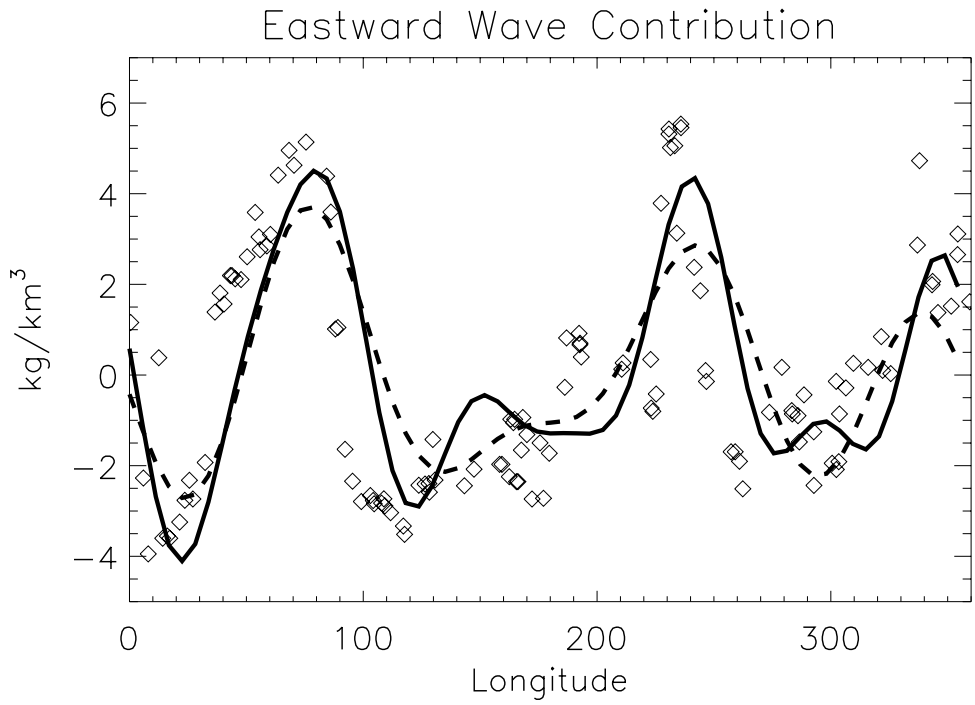

Figure 6. Contribution to the wave structure from the eastward propagating s = 1, 2 and 3 diurnal oscillations. Diamonds correspond to GCM simulations for $Ls \approx 65°$ at LT = 15 h and 115 km for the equatorial band covered by MGS observations (10S–20N) with zonal mean and migrating tides subtracted. Waves are shown as follows: dashed, sum of wave numbers one to three; solid, as dashed line with eastward semidiurnal s = 2, 3 and 5 and diurnal s = 5 added.

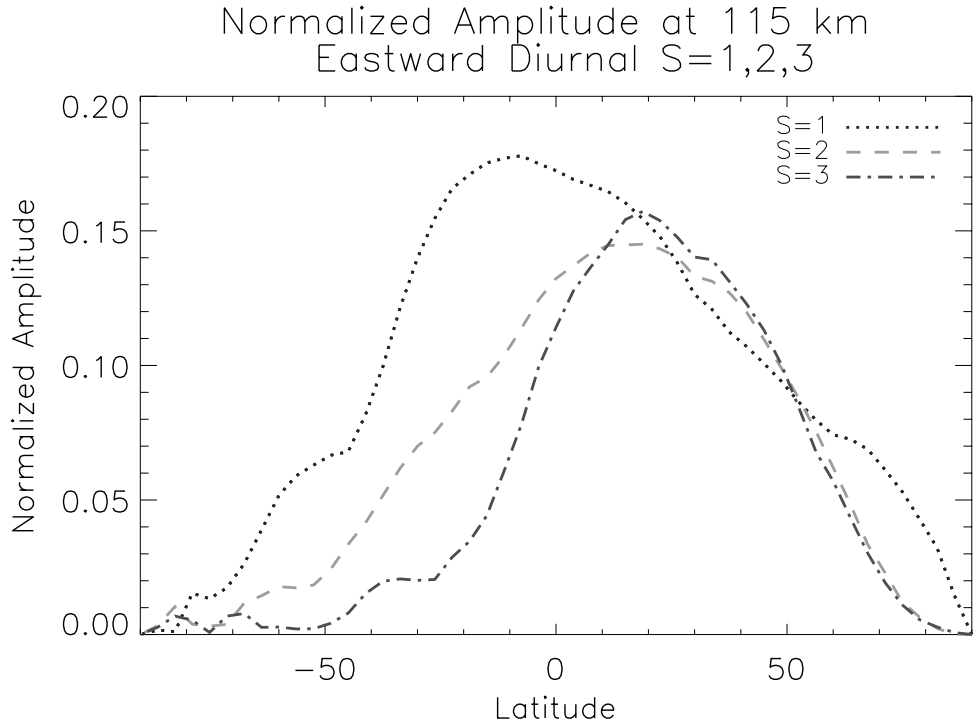

Figure 7. Relative amplitude of the eastward propagating s = 1, 2 and 3 diurnal oscillations at 115 km and $Ls \approx 65°$. Amplitudes are normalized by local zonal mean density. Horizontal axis in degrees latitude. Waves are denoted as follows: solid, s = 1; dash, s = 2; dash-dot, s = 3. See color version of this figure in the HTML.

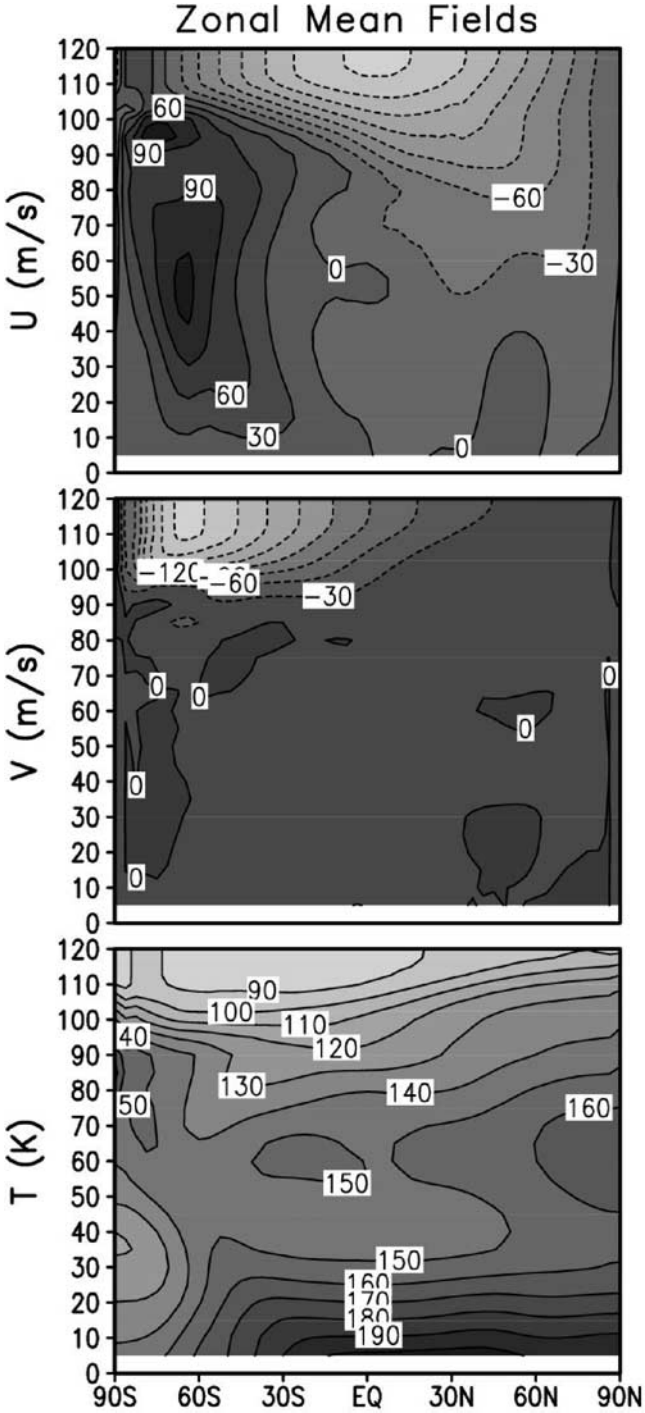

Figure 8. Latitude-altitude cross sections of zonal mean winds and temperature at $Ls \approx 65$. Top panel: Zonal mean zonal wind (positive eastward); Center panel: Zonal mean meridional wind (positive northward); Lower panel: Zonal mean Temperature.

a nonlinear interaction between already existing nonmigrating waves. Given the presence of the diurnal eastward propagating $s = 1$, 2 and 3 due to the modulation of the migrating diurnal tidal forcing by the topography in the way described in section 1, these waves can in turn participate in other interactions that could yield the diagnosed semidiurnal waves. For example, the ($\sigma = 1/12$, $s = 3$) wave could be a byproduct of the interaction between the diurnal eastward propagating waves $s = 1$ and 2. In the same fashion, the semidiurnal $s = 0$, $s = 1$ and $s = 2$ waves could be the outcome of the diurnal migrating tide interacting with the waves ($\sigma = 1/24$, $s = 1$), ($\sigma = 1/24$, $s = 2$) or ($\sigma = 1/24$, $s = 3$), respectively. The modulation of semidiurnal tidal forcing by the $s = 2,3$ component of Mars' topography has been suggested as a source for the ($\sigma = 1/12$, $s = 0$) and ($\sigma = 1/12$, $s = 1$) waves [*Forbes and Hagan*, 2000; *Wilson*, 2000; *Bougher et al.*, 2001], and probably dominates over the interaction mentioned above. The simulations performed here do not allow us to separate these two processes in relative importance, as the migrating component is necessary for both cases. The shorter wavelength semidiurnal wave with $s = 5$ could be produced through the interaction of the eastward propagating diurnal $s = 2$ and $s = 3$.

[20] An interesting outcome of these nonlinear interactions (summarized in Table 4) is the possible generation of stationary waves at high altitudes due to the presence of diurnal eastward propagating waves and migrating tides at those heights. In this way, once the eastward propagating waves reach significant amplitudes they could interact between themselves and with the migrating diurnal tide to yield stationary waves. The presence of stationary waves at those heights is evident from Figure 9, where significant amplitudes are seen above 80 km for $s = 1$, 2 and 3. From the lower atmospheric forced stationary waves only the longer wavelength $s = 1$ is expected to reach high altitudes and mostly to propagate in the eastward jet [*Hollingsworth and Barnes*, 1996]. The presence of short wavelength modes in simulations and the unexpected spatial distribution of their amplitudes hints at a possible upper atmospheric generation source. Further analysis of other simulated data at other seasons (see Forget et al., manuscript in preparation, 2003) also shows the presence of stationary waves at high altitudes and at latitudes where the eastward propagating waves with low wave number show maximum amplitudes reinforcing the possibility of this process as a source mechanism. A more extensive study to elucidate the relevance of this generation process is currently underway.

5. Role of CO_2 NIR Absorption

[21] One of the advantages of model simulations is the capability of producing a variety of different scenarios

Table 4. Possible Nonlinear Wave Interaction Mechanism as a Source of Some Waves[a]

(σ_1,s_1)	⇒	(σ_2,s_2)	⇒	(σ, s)	
(1/24, −1)		(0, 1)		(1/24, 0)	(1/24, −2)
(1/24, 1)		(0, 2)		(1/24, 3)	(1/24, −1)
(1/24, 2)		(0, 1)		(1/24, 3)	(1/24, 1)
(1/24, 2)		(0, 3)		(1/24, 5)	(1/24, −1)
(1/24, 3)		(0, 2)		(1/24, 5)	(1/24, 1)
(1/24, −1)		(1/24, 1)		(1/12, 0)	(0, 2)
(1/24, −1)		(1/24, 2)		(1/12, 1)	(0, 3)
(1/24, −1)		(1/24, 3)		(1/12, 2)	(0, 4)
(1/24, 1)		(1/24, 2)		(1/12, 3)	(0, 1)
(1/24, 1)		(1/24, 3)		(1/12, 4)	(0, 2)
(1/24, 2)		(1/24, 3)		(1/12, 5)	(0, 1)

[a]As in the text, positive (negative) wave numbers denote eastward (westward) propagating waves. Frequencies are in units of cycles/hour.

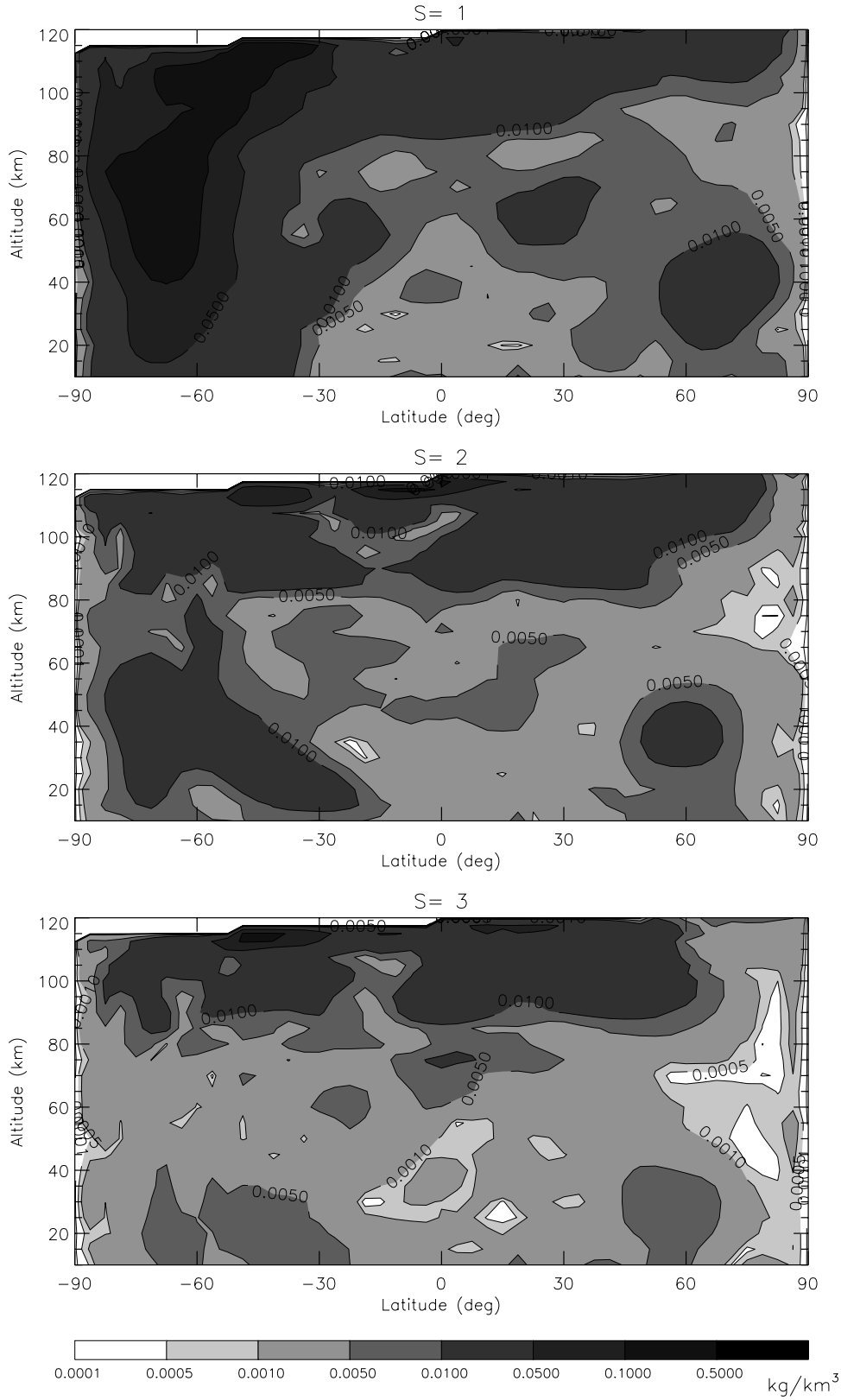

Figure 9. Relative density amplitude at $Ls \approx 65^\circ$ for stationary waves one to three present in the simulations. Amplitudes are normalized by local zonal mean values. See color version of this figure in the HTML.

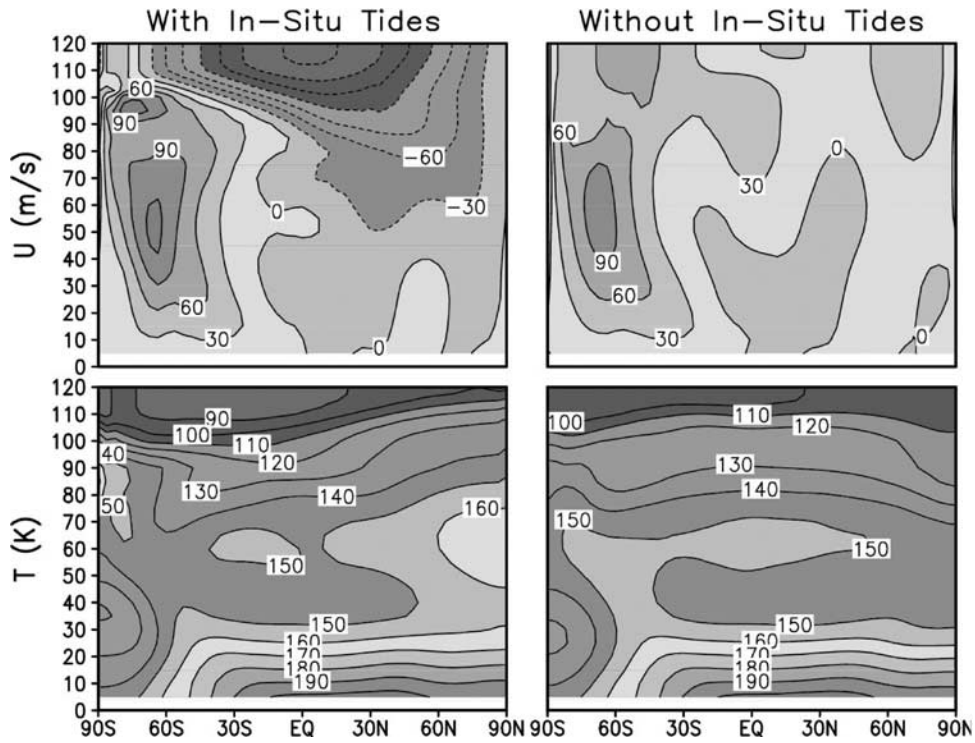

Figure 10. Latitude-altitude cross sections of zonal mean zonal wind (top) and temperature (bottom) for $Ls \approx 65°$. Left panels display full model case and right panels display no in situ thermal forcing case. Winds are in m/s and temperatures are in K. See color version of this figure in the HTML.

(realistic or not) that can help in the understanding of the big complex picture. With this in mind, a sensitivity study was performed to ascertain the role of the in situ upper atmospheric tides on the structure of the atmosphere. This scenario will also be of use in the confirmation that the diurnal eastward propagating waves obtained in the simulations are indeed Diurnal Kelvin waves.

[22] Thermal tides are forced by solar radiation absorption having two distinct sources at low and high altitudes. In the lower atmosphere the daily heat flux from the surface due to the absorption of visible radiation by the ground and the direct absorption of short wave radiation by airborne dust lead to upward propagating tides. Between approximately 80 and 120 km, the driving of in situ tidal waves can be traced to the absorption of near-IR radiation by CO_2. The differentiated nature of the forcing allows for the analysis of the effects of the two tidal wave types and their role in the total wave structure obtained. For an excellent overview of waves in terrestrial planetary atmospheres the reader is referred to *Forbes* [2002, and references therein].

[23] A simulation run was performed for the season corresponding to the MGS data presented above (Ls $\approx$ 65°) with the presence of the in situ thermal tides suppressed. This was accomplished with the use of a diurnally averaged in situ forcing while leaving all other tidal sources unmodified. The resulting heating suppressed the upper atmospheric thermal tides while maintaining the background thermal structure as close to the full model simulations as possible. Zonal mean zonal winds and temperatures obtained for this scenario are shown in Figure 10. As can be seen, the thermal structure in the absence of the in situ thermal tides closely resembles that of the full simulation case. The zonal mean zonal winds, however, are radically modified. The westerly jet in southern latitudes is decreased in magnitude and the easterlies at high altitudes disappear, giving mostly eastward winds throughout. The loss of the strong easterlies is to be expected as the solar-antisolar circulation is strongly damped with the exclusion of the in situ forcing at high altitudes. As migrating tidal amplitudes are reduced at high altitudes (see Figure 11) their participation in the induction of westward zonal mean winds is also limited adding to the loss process of easterly zonal mean winds.

[24] The obtained normalized density amplitudes when the in situ thermal tides are not present are significantly modified. Figure 11 shows normalized amplitudes for diurnal frequency waves extracted from our test-case simulation just described. The absence of in situ forcing for the migrating tides induces a lack of significant amplitude above 100 km for the $s = -1$ westward propagating component, with all the contribution being due to the lower atmospheric tidal forcing.

[25] Noticeable differences with the full-model case of Figure 4 appear in the eastward propagating waves. For all three wave numbers (one, two and three) the absence of thermal in situ tides in the upper atmosphere leads to a more equatorially symmetric response and a large decrease in amplitude for the last two waves. This difference can be ascribed to the difference in the zonal mean fields that would lead to different propagation properties for the waves. The more symmetrical distribution obtained without in situ forcing can be explained as a result of a less asymmetric zonal mean wind field (see Figure 10) which would reduce the presence of asymmetric modes induced through mode coupling on a highly asymmetric wind field.

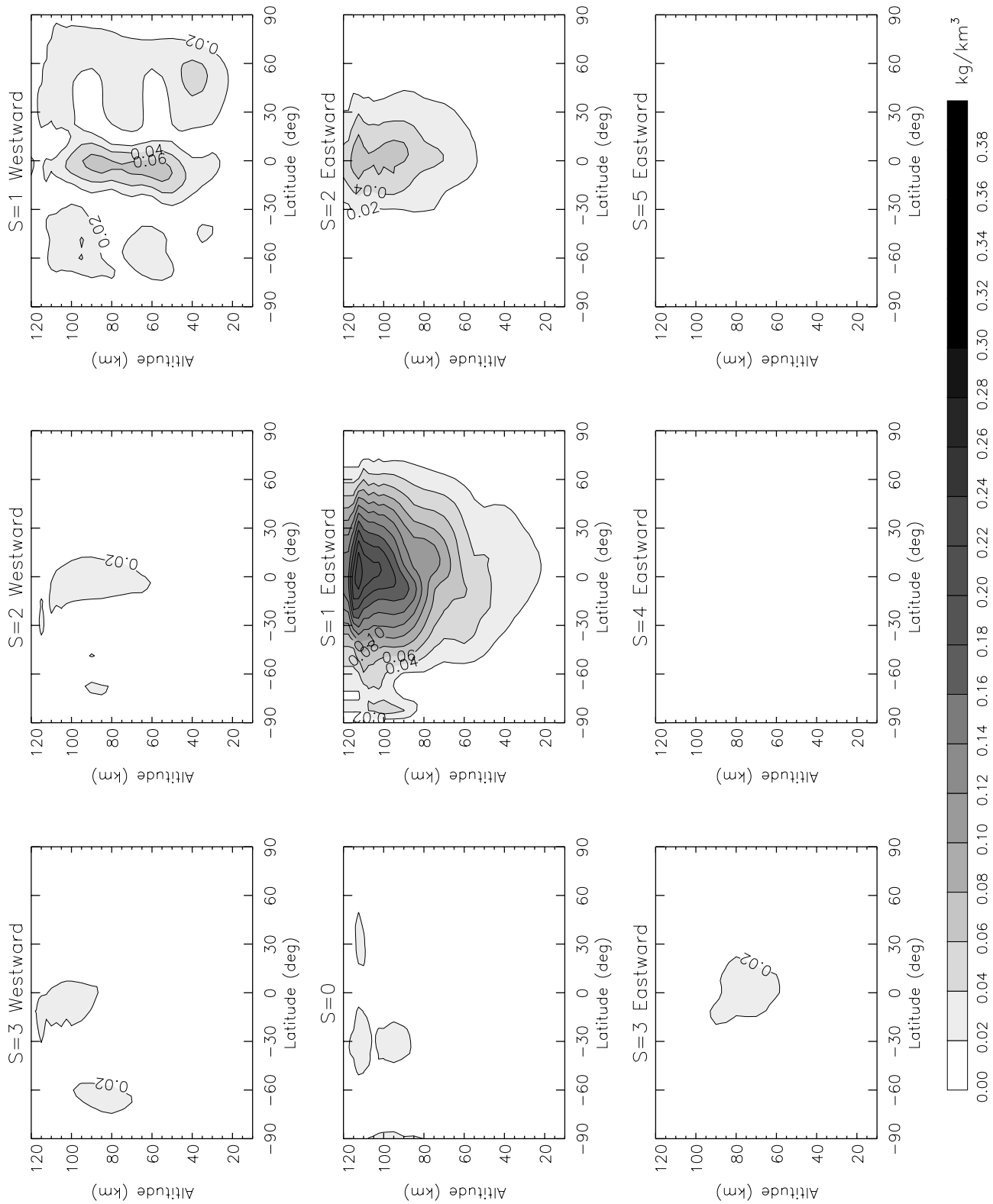

Figure 11. Relative density amplitude at $Ls \approx 65°$ for diurnal frequency waves with diurnally averaged in situ upper atmospheric heating. Amplitudes are normalized by the zonal mean values. Wave numbers range from westward propagating wave three ($s = -3$) to eastward propagating wave five ($s = 5$). See color version of this figure in the HTML.

The mostly eastward winds would then dissipate the upward propagating waves through Doppler-shifting their frequency to lower values which would increase the effect of dissipation. Thus the reduced amplitudes of waves $s = 2$ and 3 which would be more susceptible to dissipation than the wave number one due to their shorter vertical wavelengths [*Forbes et al.*, 2001]. The behavior of the diurnal eastward propagating waves observed in this study reaffirms the nature of these oscillations as diurnal Kelvin waves as has been suggested [*Forbes and Hagan*, 2000; *Wilson*, 2000, 2002; *Bougher et al.*, 2001].

[26] The relevance of mean wind interactions in the middle atmosphere in establishing the structure of the diurnal Kelvin wave $s = 1$ wave was noted by *Forbes et al.* [2001]. In their study they found that the perturbation meridional wind field obtained with no zonal mean winds above 90 km was very similar to that with non-zero zonal mean winds at all altitudes. This lead them to state that the basic asymmetric structure originated in the middle atmosphere through mean wind interactions. This is what is observed in our simulation results, where higher asymmetric modes are not strongly forced when lower/less asymmetric mean winds are present (see Figure 11) as opposed to the strongly asymmetric mean winds in the full model run (Figure 4). *Wilson and Hamilton* [1996] noted in their study of thermal tides in the Martian atmosphere that the Kelvin wave response obtained in the upper atmosphere can be significantly modified by the mean wind profile at low altitudes.

6. Summary and Conclusions

[27] LMD GCM simulations have been used to study aerobraking accelerometer data from MGS for various seasons, altitudes and latitudes. In some cases, the model simulations fare very well in the comparison with the observed data which allows for its use in its analysis. Results show better agreement at mid to low latitudes, while high latitude comparisons present larger differences between the modeled and observed data. These differences are ascribed to an underestimation of the atmospheric temperature at low altitudes in the polar regions, the high day-to-day variability obtained at high latitudes in the simulated data and the fact that the simulated data are averaged over 10 days. This transient behavior has to be further studied and will be addressed in a separate analysis. Dust storm season results reproduce the main features observed by MGS, although few discrepancies are thought to relate to differences in the dust distribution in the simulations.

[28] We have focused on MGS data, obtained at constant local time for Ls $\approx 65^\circ$ at an altitude of 115 km. These observations are well reproduced in the LMD GCM results. The model clearly simulates the planetary-wave structure seen in the observed data. The sampling at a single local time of waves in the atmosphere renders impossible the extraction of the different wave components from the observations since a variety of wave number-frequency combinations can yield a certain signature when sampled at a constant local time. This makes the use of model simulations an invaluable tool in the understanding of observations.

[29] Space-time Fourier decomposition of the simulation data yields the diurnal eastward propagating waves with wave number one, two and three as the major contributors to the structure observed by MGS at equatorial latitudes. These waves are concentrated at low latitudes and peak above 100 km. This structure is highly indicative of the nature of these waves as diurnal Kelvin waves. The major source of diurnal Kelvin waves is the modulation of lower atmospheric heating by longitudinal topographic variations. Further test-case simulations performed without the presence of in situ forcing at high altitudes due to near-infrared absorption by CO_2 confirm that these waves originate in the low atmosphere. Without the high altitude thermal forcing the waves are found to be more equatorially trapped and display less latitudinal asymmetries. Magnitudes are also found to be lower for wave numbers two and three. Both of these effects are ascribed to their propagation through a less asymmetric and more eastward zonal mean zonal wind field when the upper heating source is not included. The reduced asymmetry in the mean zonal wind reduces the mode coupling into higher asymmetric modes and the predominantly eastward winds increase the effect of dissipation on the shorter vertical wavelength waves. This behavior is highly indicative of diurnal Kelvin waves and therefore confirms the interpretation.

[30] Other significant waves required to match the observations in our simulations are the semidiurnal eastward propagating waves with wave numbers two, three and five and the diurnal eastward propagating wave with $s = 5$. These waves help create the density peak at a longitude of 230°E seen in the data (see Figure 3a). It is striking that such a combination of minor waves can increase the density encountered by a spacecraft by almost 40%. This illustrates the complex nature of the Martian atmosphere at those heights and the need for further observations and continuing modeling efforts. Possible nonlinear mechanisms that could generate the main waves obtained in the analysis are suggested, but given the complexities of GCM models a mechanistic approach is required to ascertain the relative importance of these processes.

[31] **Acknowledgments.** This research was funded under CNES Mars Premier Program and ESTEC Contract 11369/95/NL/J. The authors would like to thank Jeff Forbes, John Wilson and Paul Withers for their suggestions and comments, and Gerry Keating and the MGS team for the use of the in situ data. Much appreciated modeling support was provided by Yann Wanherdrick.

References

Andrews, D. G., J. R. Holton, and C. B. Leovy (1987), *Middle Atmospheric Dynamics*, Academic, San Diego, Calif.

Angelats i Coll, M., and J. M. Forbes (2002), Nonlinear interactions in the upper atmosphere: The s = 1 and s = 3 nonmigrating semidiurnal tides, *J. Geophys. Res.*, *107*(A8),1157, doi:10.1029/2001JA900179.

Bougher, S., S. Engel, D. P. Hinson, and J. M. Forbes (2001), Mars Global Surveyor radio science electron density profiles: Neutral atmosphere implications, *Geophys. Res. Lett.*, *28*, 3091–3094.

Conrath, B. (1976), Influence of planetary-scale topography on the diurnal thermal tide during the 1971 Martian dust storm, *J. Atmos. Sci.*, *33*, 2430–2439.

Forbes, J., and M. Hagan (2000), Diurnal Kelvin wave in the atmosphere of Mars: Towards an understanding of 'stationary' density structures observed by the MGS accelerometer, *Geophys. Res. Lett.*, *27*, 3563–3566.

Forbes, J. M. (2002), Wave coupling in terrestrial planetary atmospheres, in *Atmospheres in the Solar System: Comparative Aeronomy*, *Geophys. Monogr. Ser.*, vol. 130, pp. 171–190, edited by M. Mendillo, A. Nagy, and J. H. Waite, AGU, Washington, D. C.

Forbes, J., N. A. Makarov, and Y. I. Portnyagin (1995), First results from the meteor radar at south pole: A large 12-hour oscillation with zonal wavenumber one, *Geophys. Res. Lett.*, *22*, 3247–3250.

Forbes, J. M., M. E. Hagan, S. W. Bougher, and J. L. Hollingsworth (2001), Kelvin wave propagation in the upper atmospheres of Mars and Earth, *Adv. Space Res.*, *27*(11), 1791–1800.

Forget, F., F. Hourdin, R. Fournier, C. Hourdin, O. Talagrand, M. Collins, S. R. Lewis, P. L. Read, and J.-P. Huot (1999), Improved general circulation models of the Martian atmosphere from the surface to above 80 km, *J. Geophys. Res.*, *104*, 24,155–24,176.

Hollingsworth, J., and J. Barnes (1996), Forced stationary planetary waves in Mars' winter atmosphere, *J. Atmos. Sci.*, *53*, 428–448.

Hourdin, F., P. Le Van, F. Forget, and O. Talagrand (1993), Meteorological variability and the annual surface pressure cycle on Mars, *J. Atmos. Sci.*, *50*, 3625–3640.

Keating, G., et al. (1998), The structure of the upper atmosphere of Mars: In situ accelerometer measurements from Mars Global Surveyor, *Science*, *279*, 1672–1676.

Keating, G. M., R. H. Tolson, J. L. Hanna, R. F. Beebe, J. R. Murphy, and L. F. Huber (2001), *MGS-M-ACCEL-5-ALTITUDE-V1.0*, NASA Planet. Data Syst., Jet Propul Lab., Pasadena, Calif.

Teitelbaum, H., and F. Vial (1991), On tidal variability by nonlinear interaction with planetary waves, *J. Geophys. Res.*, *96*, 14,169–14,178.

Wilson, R. (2000), Evidence for diurnal period Kelvin waves in the Martian atmosphere from Mars Global Surveyor TES data, *Geophys. Res. Lett.*, *27*, 3889–3892.

Wilson, R. J. (2002), Evidence for nonmigrating thermal tides in the Mars upper atmosphere from the Mars Global Surveyor Accelerometer Experiment, *Geophys. Res. Lett.*, *29*(7), 1120, doi:10.1029/2001GL013975.

Wilson, R., and K. Hamilton (1996), Comprehensive model simulation of thermal tides in the Martian atmosphere, *J. Atmos. Sci.*, *53*, 1290–1326.

Withers, P., S. W. Bougher, and G. M. Keating (2003), The effects of topographically-controlled thermal tides in the Martian upper atmosphere as seen by the MGS accelerometer, *Icarus*, *164*(1), 14–32.

Zurek, R. (1976), Diurnal tide in the Martian atmosphere, *J. Atmos. Sci.*, *33*, 321–337.

M. Angelats i Coll and F. Forget, Laboratoire de Météorologie Dynamique, CNRS, Université Paris 6, Tour 25, 5ème étage, B.P. 99, 4, place Jussieu, 75231, Paris Cedex 05, France. (malmd@lmd.jussieu.fr)

M. A. López-Valverde, Instituto de Astrofisica de Andalucía, Granada, Spain.

S. R. Lewis and P. L. Read, Atmospheric, Oceanic and Planetary Physics, University of Oxford, Clarendon Laboratory, Parks Road, Oxford, UK.